Electronic Supplementary Information

S1 Supporting figures

S1.1 Synthesis and characterisation of polymers

Analytical Methods: Nuclear Magnetic Resonance Spectroscopy was performed on a Bruker AV-400 NMR machine (400 MHz) in $CDCl_3$. ^{1}H NMR was recorded in the range 0 - 10 ppm against a TMS reference. Regioregularity was determined from the methylene proton integrals at 2.50 - 2.60 ppm (ir) and 2.75 - 2.84 ppm (r) using the formula: $\frac{r}{(ir+r)} \times 100$ %. UV-Visible absorption spectra were measured using a Fluoromax-2 fluorimeter fitted with a transmission detector. Refractive Index Size-Exclusion Chromatography (RI-SEC) was performed using an Agilent 1200 Series GPC-SEC Analysis System fitted with two PLgel mixed-B columns in series running a chlorobenzene eluent and calibrated to polystyrene standards. Samples were dissolved in chlorobenzene and filtered with a 0.2 μm PTFE filter to remove particulate matter. Polymer eluted between 14 and 18 minutes.

Synthesis of P3HT-*block*-P3EHT: 0.49 g (1.5 mmol) of 2,5-dibromo-3-hexylthiophene (Lanzhou Galaxy) was degassed in an oven-baked flask. The flask was recharged with argon and 10 mL of freshly distilled THF were added. Next, 0.75 mL (1.5 mmol, 1 equiv.) of 2M isopropylmagnesium chloride (Aldrich) was added by dropwise addition. The solution was heated to 45 °C for 30 minutes to ensure full conversion of the monomer to the thienyl-Grignard. The polymerisation was initiated by the addition of 44 mg (8.1 mol, 2.7 mol% overall) of 1,3-bis[diphenylphosphinopropane]nickel(II) chloride. The solution was stirred at 45 °C for a further 120 minutes. In a separate oven-baked flask, the 3-(2-ethyl)hexylthiophene thienyl-Grignard solution was prepared in an analogous fashion to the above with 0.53 g (1.5 mmol) of 2,5-dibromo-3-(2-ethyl)hexylthiophene (prepared using literature methods [1,2]).

After 120 minutes had passed for the initial polymerisation a 1 mL aliquot was removed and quenched (M_p 3.8 kg/mol). The second thienyl-Grignard solution was then hot injected into the first flask (minus 1 mL to maintain a 50:50 feed ratio). The reaction was left to stir for a further 120 minutes at 45 °C, after which the polymer was quenched with excess cold methanol yielding a purple solid. The polymer was filtered by gravity and then purified using Soxhlet purification in methanol and then extracted into chloroform. The final polymer was found to have be M_n 5.9 kg/mol, M_w 11.0 kg/mol, PDI 1.8 (M_p 7.0 kg/mol), see Fig. S1. ^{1}H NMR (400 MHz, $CDCl_3$): δ 7.00 (s, Ha), 6.97 (s, Ha'), 2.83 (dt, Hb), 2.75 (dd, Hb'), 1.73 (m, Hc/Hc'), 1.53-1.15 (m, Hd/Hd'/Hd''/He/He'/He''/Hf/Hf'), 0.94 - 0.91 (m, Hg/Hg'), see Fig. S1.

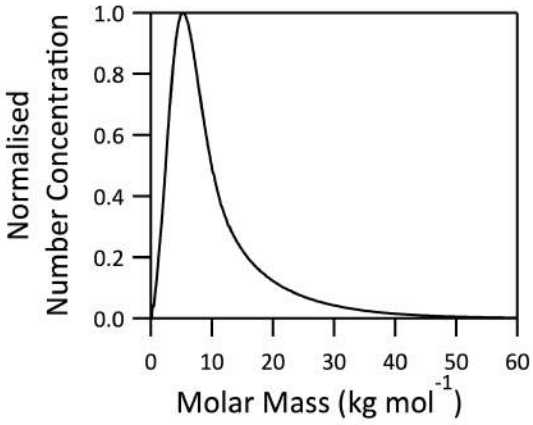

Fig. S1 RI-SEC trace of P3HT-*b*-P3EHT, showing the distribution of polymer chain lengths.

Figure S2a shows the full range ^{1}H NMR for the P3HT-*b*-P3EHT block copolymer. Due to the chemical similarities between the two species, the signals from comparable proton regions overlap. Figures S2b and S2c show close ups of the ring proton and methylene peaks respectively. Overlaid onto each figure are the two corresponding homopolymer spectra. In each case the characteristic features of each homopolymer appear in the block copolymer spectrum, confirming the block copolymer nature of the material (in the case of a random copolymer a set of four peaks is expected for each combination of hetero/homo coupling [3]).

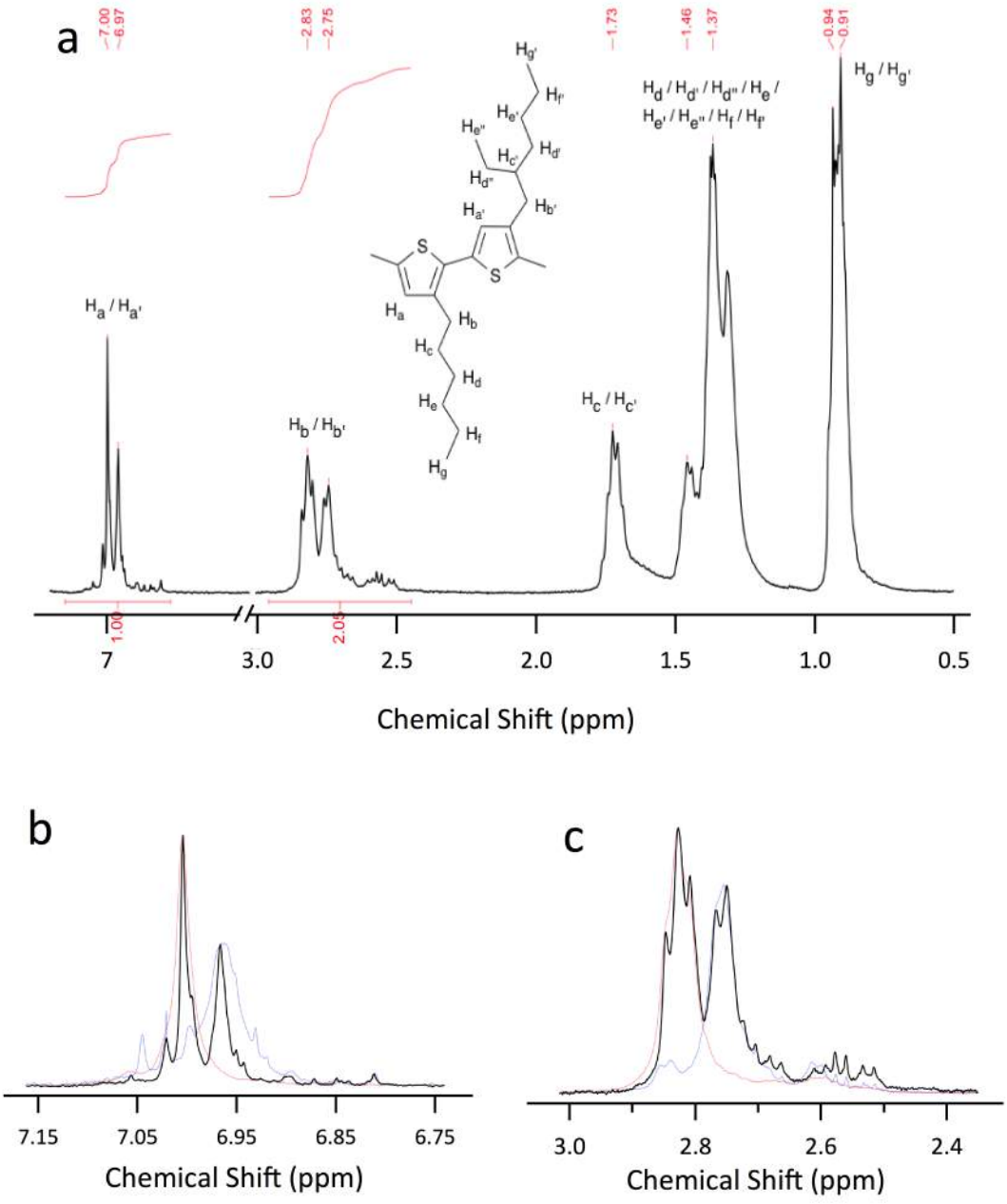

Figure S2. ^{1}H NMR spectrum of P3HT-*b*-P3EHT. (a) Full spectrum (b) Detail of ring proton region (Ha and Ha') in ^{1}H NMR spectrum (c) Detail of methylene region (Hb and Hb'); (—) P3HT-*b*-P3EHT, (—) P3HT and (—) P3EHT.

Determining the absolute block ratio of these materials is complicated by the overlapping signals in the NMR,

which prevents direct comparison of individual signal integrals. Instead we use a fitting method on the methylene region with the two homopolymers to determine an approximate ratio. By first normalizing and then scaling the NMR spectrum of the two homopolymers to match the respective peak height in the block copolymer spectrum, as depicted in Fig. S2b, it is then possible to compare the respective integrals. Using this method a ratio of 54:46 3-HT:3-EHT was determined.

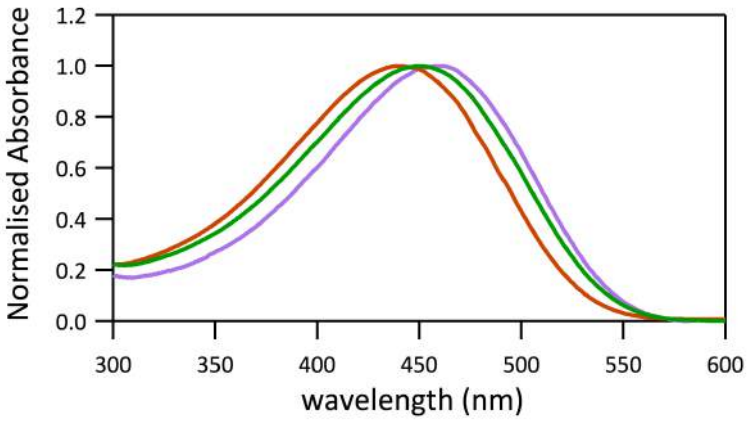

Fig. S3 Solution absorption spectra of all three polymers in chlorobenzene: (—) P3HT, (—) P3HT-*b*-P3EHT and (—) P3EHT.

The solution absorption spectra of all three polymers were recorded in chlorobenzene, shown in Fig. S3. P3HT-*b*-P3EHT was found to exhibit a peak absorbance at 450 nm in between that of the P3HT (460 nm) and P3EHT (442 nm) homopolymers, as expected for a copolymer. The characteristics of each polymer are summarised in Table S1.

	UV-visible Absorption Spectra				
Material	Peak Wavelength (nm)	FWHM (nm)	M_w (kg mol^{-1})	PDI	RR (%)
P3HT	460	123	20	1.8	89
P3EHT	442	127	16	1.7	90
P3HT-*b*-P3EHT	450	129	11	1.8	—

Table S1 Physical properties of the polymers

Binary blends of P3HT-*b*-P3EHT and PCBM were prepared with PCBM fractions ranging from 0 to 65 wt%. The fraction of each blend is listed in Table S2. Sample names are given by BXX to denote that blends are binary, composed of P3HT-*b*-P3EHT and PCBM, with XX weight percentage PCBM.

Sample Name	Weight Fraction PCBM
diblock	0.000
B05	0.050
B10	0.101
B35	0.339
B40	0.404
B50	0.493
B65	0.652
PCBM	1.000

Table S2 Sample names and PCBM weight fractions.

S1.2 DSC measurements of T_g for pure components

Glass transition temperatures were measured for each of the pure components: PCBM, P3HT (20 Kg/mol), P3EHT (16 Kg/mol), and P3HT-b-P3EHT (11 Kg/mol) as shown in Figure S4. The T_g of PCBM, 130 °C, appears as a weak inflection in the heat capacity profile measured for a heating ramp of 10 °C/min. The sample was prepared by melting for 5 min at 300°C, and then quenching to -50°C. This value is in agreement with the more pronounced T_g measured by Zhao et al. by ageing the PCBM and quenching it prior to the heating ramp[4]. An exothermic peak at 177 °C is identified as the cold crystallisation temperature, T_{cc}. The T_g's of the polymers were measured by ageing the samples at room temperature for a day and then quenching them to -50°C. A ramp rate of 10°C was used for all samples. The T_g of P3EHT is around 9°C, and double melting peaks, consistent with crystal polymorphs observed by Ho et al.[2] melt at 81°C. The T_g of P3HT is around -9°C, coincident with a shallow exothermic baseline that indicates cold crystallisation. The endothermic transition around 60°C has previously been identified as the alkyl side chains melting[5]. The diblock copolymer exhibits a T_g around -2°C, reasonably between those of the two homopolymers, and an endothermic transition around 63°C. We have identified the endotherm as melting of the alkyl side chains in P3HT crystals because GIWAXS measurements have confirmed that the P3EHT block remains amorphous.

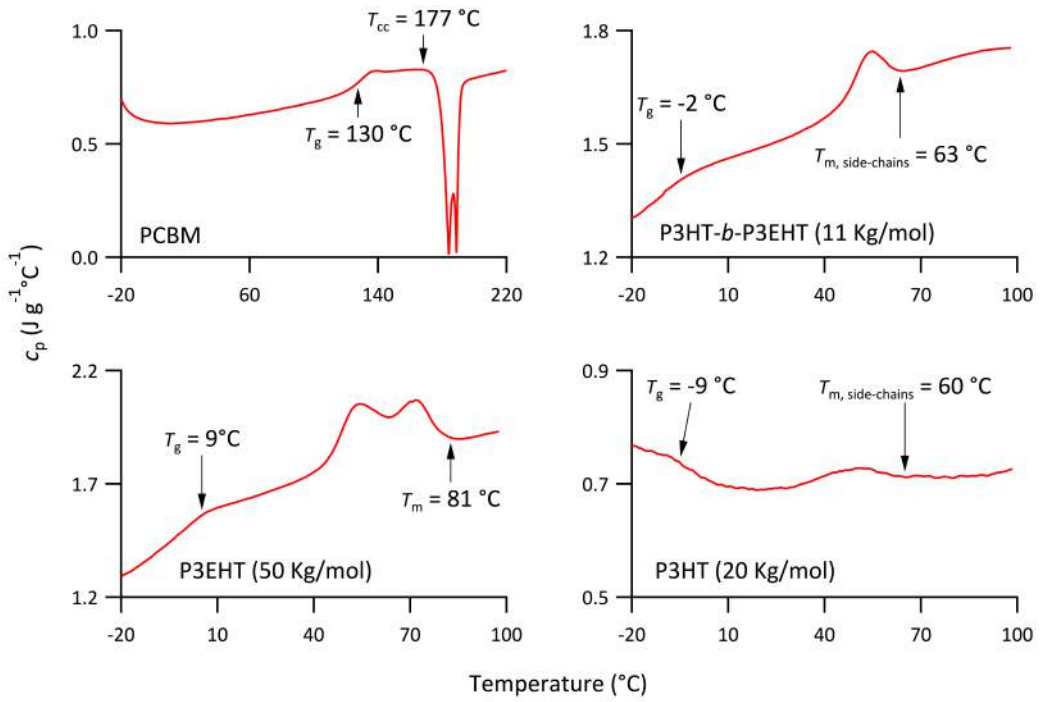

Fig. S4 DSC specific heat capacity profiles for pure components indicating the measured T_g. All samples were measured whilst heating at 10 °C/min. The PCBM was prepared by quenching from the melt and the polymers were all quenched from 25 to -50°C.

S1.3 GIWAXS geometry, 2D spectra, and radially integrated spectra

The grazing incidence geometry is shown schematically in Figure S5 to illustrate the Cartesian sample coordinate system ($x^{'}$, $y^{'}$, $z^{'}$), the Cartesian detector coordinate system (q_{xy}, q_z), and the spherical coordinate system for scattering events (k, α_f, θ_f). The components of the momentum transfer vector, $\boldsymbol{q}$, are defined relative to the sample geometry: $q_x^{'}$ is in the direction of the incident beam, $q_y^{'}$ is in the plane of the sample perpendicular to the beam, and $q_z^{'}$ is out of the plane of the sample.

$$\boldsymbol{q} = \boldsymbol{k}_f - \boldsymbol{k}_i = \begin{cases} cos\alpha_f cos2\theta_f - cos\alpha_f \\ cos\alpha_f sin2\theta_f \\ sin\alpha_i + sin\alpha_f \end{cases}$$

The scattered angle, α_f is measured with respect to the sample surface and the scattered angle, θ_f, is measured with respect to the plane of incidence. Figure S5 illustrates the conventions of the sample geometry. For ease of analysis, $\boldsymbol{q}$ is presented relative to the detector coordinate system with components q_{xy} and q_z. The scalar value used in 1D integrated profiles is given by: $q = \sqrt{q_z^2 + q_{xy}^2}$.

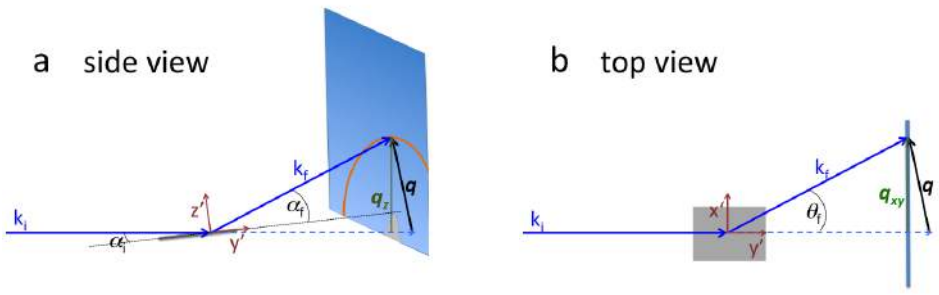

Fig. S5 Schematic geometry of the GIWAXS experiment. (a) side view showing a scattering event that is entirely within the plane of incidence (no q_{xy} component). (b) top view of the scattering geometry showing a scattering event that is orthogonal to the plane of incidence (no q_z component).

The uncorrected 2D spectra are shown for selected samples in Figure S6. The (100) diffraction ring for monoclinic P3HT, located at $q = 3.9$ nm^{-1}, is evident in the neat diblock copolymer and all of the blends, however is weak due to the low P3HT content in the samples. PCBM crystals formed from solutions of chlorobenzene are known to exhibit a triclinic lattice, likely due to intercalation of solvent into the PCBM crystal[6]. Characteristic PCBM diffraction peaks are evident in blends B50 and B65, both of which are above x_{misc}.

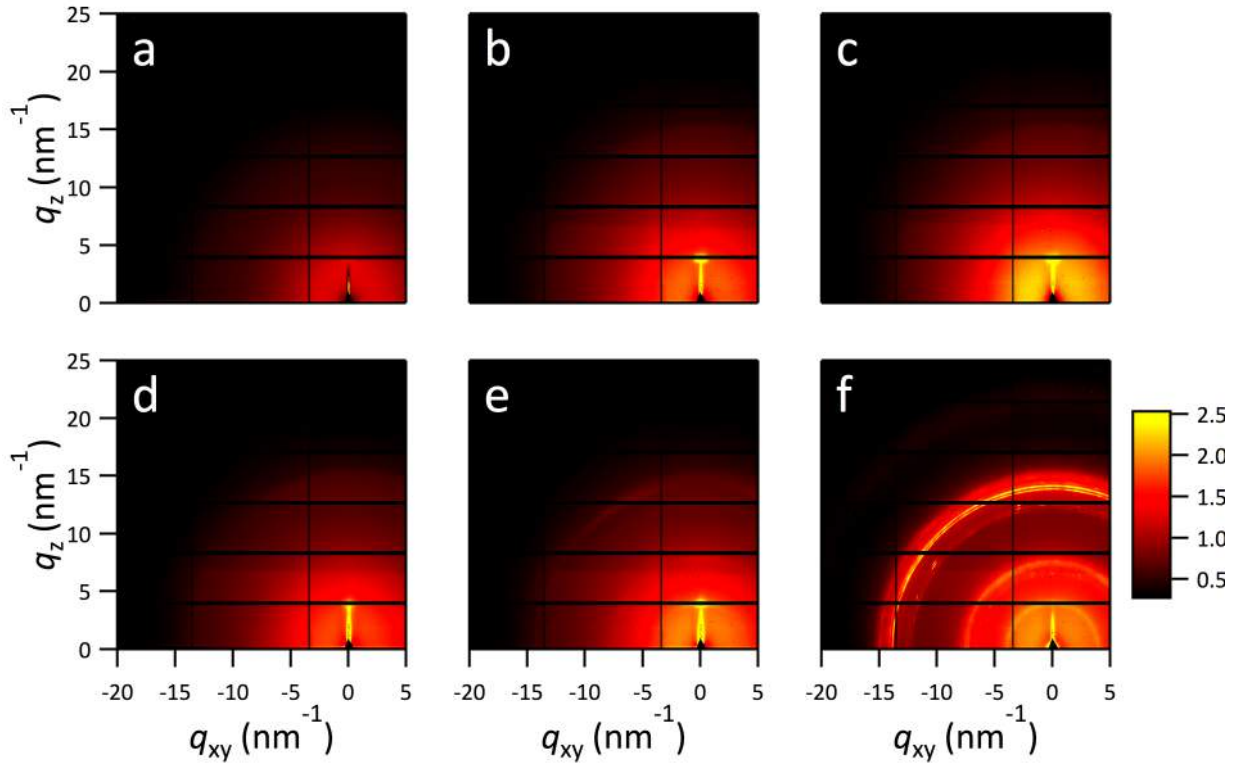

Figure S6. GIWAXS spectra (uncorrected) for thin films of P3HT-*b*-P3EHT, PCBM, and blends thereof: (a) pure diblock copolymer, (b) B05, (c) B10, (d) B50, (e) B65, (f) pure PCBM. The heat map scale shown to the left of (f) gives the raw intensity scaling multiplied by 10^{-5} in arbitrary units, it applies to all spectra.

The spectra shown in Figure S6 were radially integrated in a "pie sector" about the q_z axis to produce an I vs q meridian, and in pie sectors about the q_{xy} axis to produce equators. Meridians were integrated over the range $\bar{\chi} = [\frac{3\pi}{7}, \frac{\pi}{2}]$, largely capturing (h00) diffraction from edge-on P3HT crystals. Equators were integrated over the range $\bar{\chi} = [0, \frac{\pi}{14}]$, predominantly capturing face-on crystalline features and the (020) π-π stacking from edge-on crystals. Partial pole figures were constructed by integrating an annular region of width spanning one standard deviation on either side of the (100) P3HT peak (q = 3.63 - 4.20 nm^{-1}), as a function of $\bar{\chi}$. In practice, all reported intensity values are the sum of pixel values in the region of integration, normalised by the number of pixels counted.

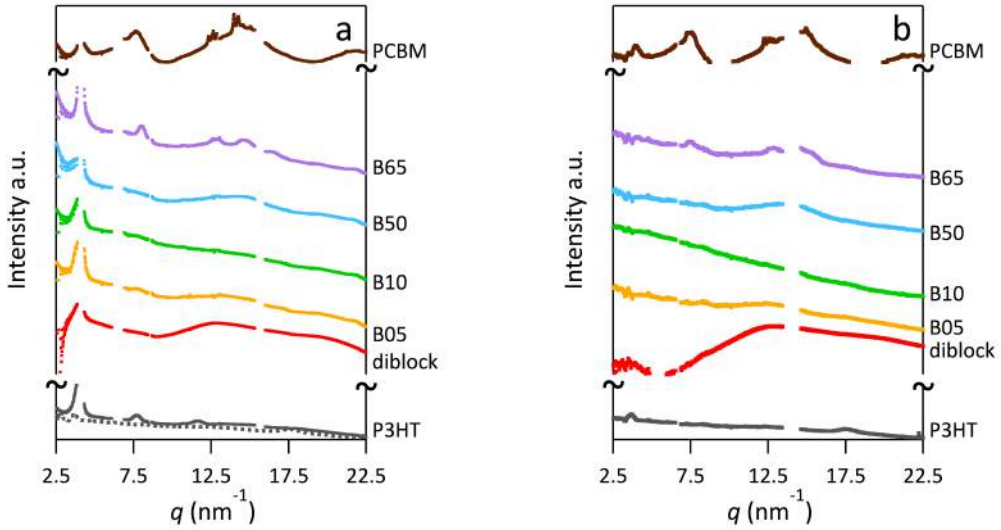

Fig. S7 Radially integrated GIWAXS spectra for P3HT, PCBM, P3HT-*b*-P3EHT, and P3HT-*b*-P3EHT:PCBM blends. (a) Meridians (b) Equators.

Figure S7 shows meridians and equators for selected samples. Unique to PCBM, the meridian and equator very nearly overlap, indicating isotropically oriented crystals. In contrast, the meridian and equator vary dramatically for P3HT because the crystals are anisotropically oriented. Because the scattering signal is weak, it is difficult to identify the onset of PCBM diffraction peaks in blended samples. The amorphous halos of PCBM and P3HT are both in the vicinity of 14 nm^{-1}, and are indistinguishable from one another.

S1.4 AFM height and phase images and 2-D DFT's

AFM images for the entire series of P3HT-*b*-P3EHT blends is shown in Figure S8. Side-by-side comparison of the height and phase AFM images shows a decoupling of topographical features in the film and the regular block copolymer nanostructure. Although nanostructured features are apparent in some of the height images, it is not clear whether they are due to machine coupling of the signals or whether they accurately depict small variations in the height. The phase images were chosen for DFT analysis, and the entire power spectra are shown in the bottom row of S8.

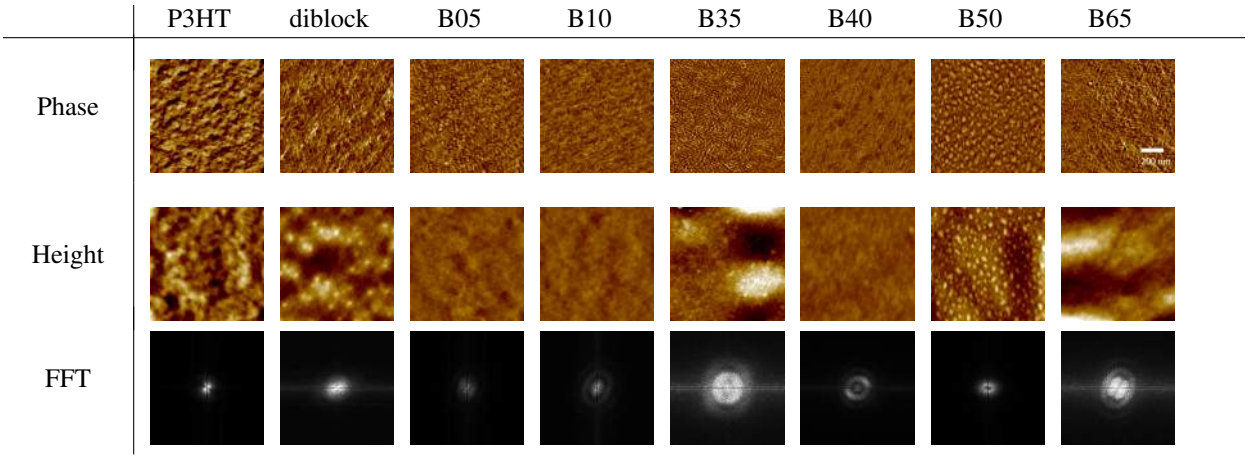

Figure S8. AFM images for P3HT-*b*-P3EHT:PCBM blends and for neat P3HT homopolymer. The row of FFT images is calculated from the real space phase image. The scale bar designated in the phase image of B65 applies to all real space images (height and phase).

S1.5 Microscopic surface features

Microscopic PCBM crystals formed on the surfaces of all blends for which the PCBM fraction was greater than x_{misc}. Figure S9 shows low and high magnification optical micrographs for all of these blends. Blend B35 has the lowest loading of PCBM studied for which microscopic crystals were observed. The rough features shown in the 5x image are mostly due to the large scale surface modulations of the film, whilst the small light-coloured features ringed in blue are the microscopic PCBM crystals that are apparent in the 100x image. In all cases, the PCBM crystals are surrounded by a "hole" from which the diblock copolymer film has retracted. These holes are optically visible as dark regions. AFM height measurements indicate that the polymer film in a "hole" region is the same thickness as the PEDOT:PSS under layer, suggesting that the diblock copolymer film completely retracts in the region of a growing PCBM crystal. The structure of the microscopic PCBM crystals is exceptionally anisotropic, growing to 10's of microns in the plane of the film, and ˜150 nm out of plane (1.5 times the original film thickness). However there is evidence that PCBM crystals also grow out of the plane of the film (see Figure S11).

The number density of microscopically observable PCBM crystals increases as a power law of the PCBM fraction, as shown in Figure S10b. The logarithmic relationship between the number of nucleation sites formed and the concentration of PCBM suggests a Brownian mechanism for nucleation, consistent with freely mobile PCBM molecules diffusing through a polymer medium. In addition to higher primary nucleation rates, the evidence of increased crystal branching for PCBM crystals in blends B50 and B65 may be due to secondary nucleation.

Surface undulations vary dramatically with PCBM content as shown in the bottom row of Figure S9. The average height of undulations, δh_u is quantified with AFM, and the surface area of the film that exhibits raised regions, A_u, is quantified using a combination of thresholded OM and AFM images. Finally, a rough estimate of the undulated volume of the sample is calculated from $V_u = A_u h_u$. Figure S10a shows that V_u increases in a roughly linear fashion with PCBM loading. At the highest loading of PCBM studied, B65, the film is dominated by microscopic PCBM crystals, surrounded by irregularly shaped polymer-rich regions. Under optical microscopy the polymer islands do not appear to be modulated, but examination under AFM reveals a very fine length scale modulation of the polymer film as seen in Figure S9.

This data clearly demonstrates that the trends in V_u and ρ_N are due to the fraction of PCBM in thin film blends, and the simultaneous occurrences of PCBM crystallisation and surface undulation (see Figure S13) imply a causal relationship. We have proposed that PCBM crystals growing out of the plane of the film draw the polymer up, resulting in the undulations. The basis for this hypothesis derives largely from AFM images of undulated, crystallised films, like the ones shown in Figure S11. A series of height and phase AFM images capture the different length scales of features on the modulated surface of blend B50. Arrows indicate the features that we suspect are PCBM crystals growing out of the plane of the film. These features are strongly apparent in both height and phase images, emerging about 10 nm

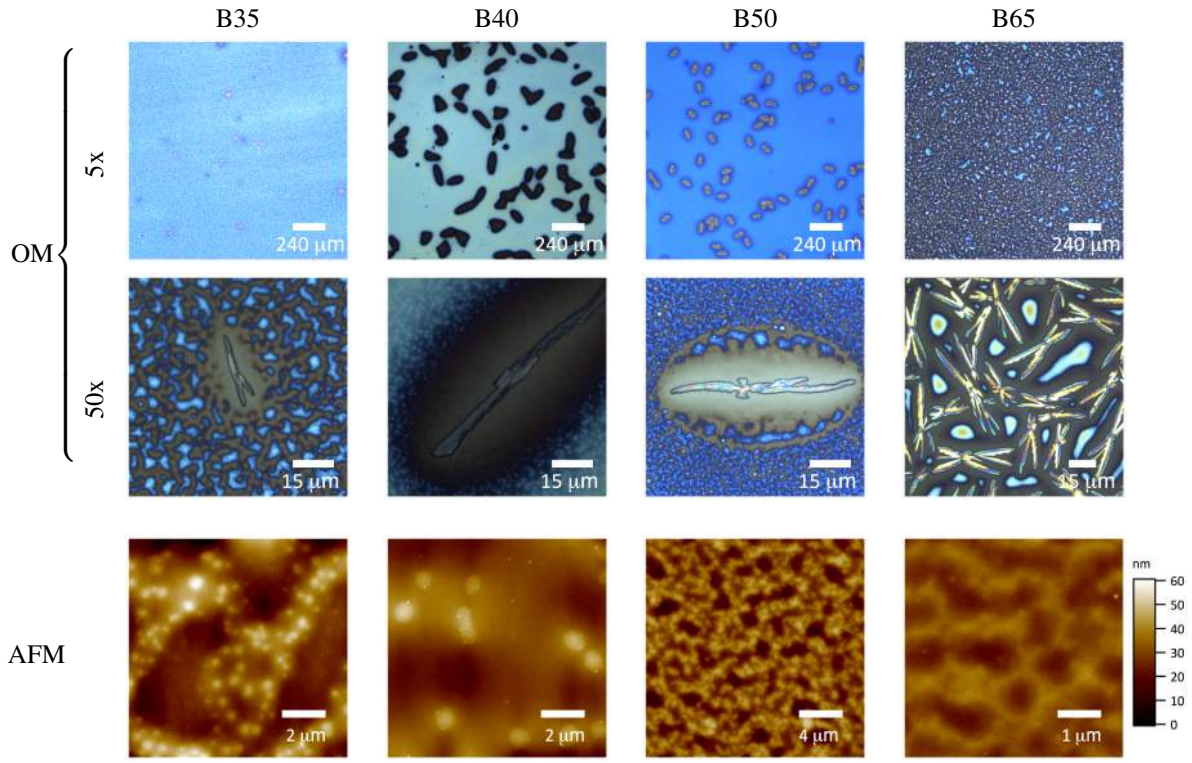

Figure S9. Surface features for P3HT-*b*-P3EHT:PCBM blends with PCBM fractions exceeding x_{misc}. Optical micrographs show PCBM crystals on the top surface of the films: the area coverage of crystals is apparent for 5x magnification and details of the PCBM crystal and surrounding film are apparent for 100x magnification. AFM images detail the surface undulations; the colour scale bar applies to all AFM images.

out of the surrounding, undulated film surface. These crystals appear predominantly in undulated regions of the film, especially near the edges of raised undulations, which is one reason why we suspect a causal relationship.

It is noteworthy that the large-scale surface undulations, evident in the height images, appear relatively flat in the phase images, indicating that there is not a significant change in the elastic modulus of the film in flat and undulated regions. The entire undulated surface is covered in nanophase separated structures, suggesting that the ordering of the diblock copolymer happens sequentially after the undulation of the film surface. The ordering of the copolymer appears to be highly robust to undulations on the film surface, supporting our assertion that the bottom substrate directs nanophase separation (rather than the top, free interface).

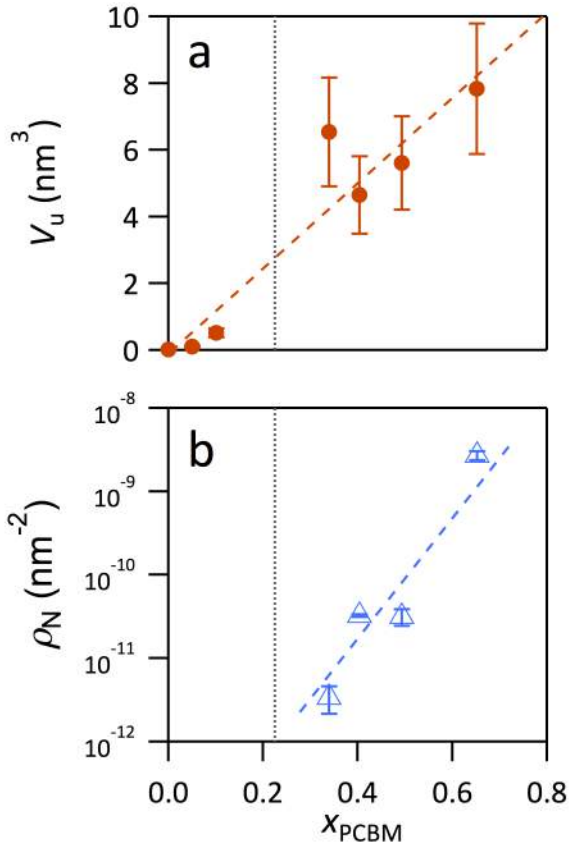

Fig. S10 Trends in the microscopic film properties of P3HT-*b*-P3EHT:PCBM blends as a function of PCBM fraction: (a) the undulated volume, V_u, of polymer-rich regions (•). The dashed line (- - -) is a linear fit to the data. (b) The number density of PCBM crystals, ρ_N (△). The dashed line (- - -) is a power law fit to the data. The vertical dashed line in both (a) and (b) indicates the approximate position of x_{misc}

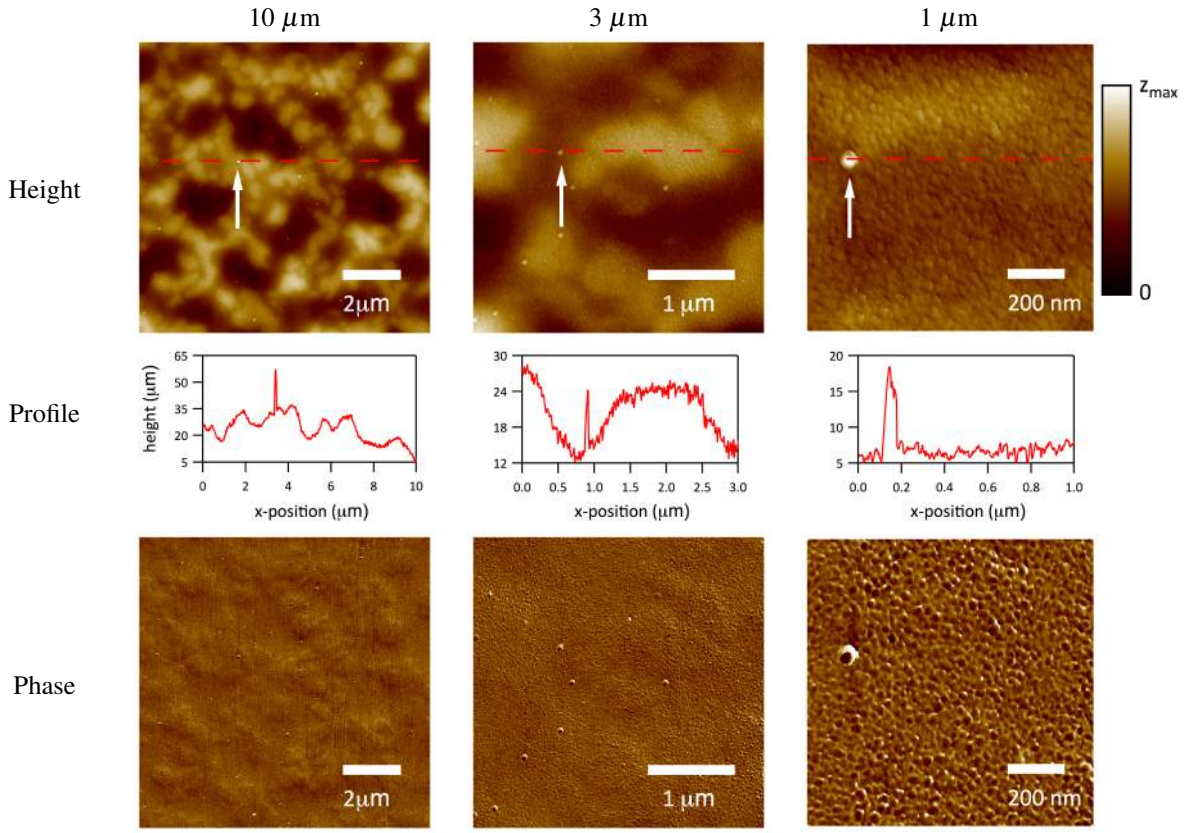

Figure S11. Atomic Force Micrographs of B50, a 50:50 blend of P3HT-*b*-P3EHT:PCBM, at various magnifications. Arrows indicate features that are likely to be PCBM crystals. The total scan size is indicated above the images, for utility a scale bar is also placed onto each image. The dashed line the height images shows the path used to obtain the vertical profile of the film surface that is shown directly below the image. The colour mapping of the phase image varies strongly with experimental parameters (like the age of the AFM tip used) and was adjusted for visual contrast. The colour mapping of the height image is given for each magnification by the scale bar on the right: for 10 μm z_{max} = 60 nm, for 3 μm z_{max} = 40 nm, and for 1 μm z_{max} = 10 nm.

S1.6 Dynamic annealing studies of micro- and nanostructure in thin films

S1.6.1 Nucleation rate of microscopic PCBM crystals.

The progression of PCBM crystal growth in blend B35 was was studied at 120 °C, significantly reduced from T_{anneal} = 200 °C, in order to slow the kinetics of crystallisation to a measurable time frame. Figure S12 shows a time series of optical micrographs and the trend in the number density of microscopically observable nucleation sites, ρ_N, with time. Under the isothermal annealing conditions used, the rate of nucleation is constant, giving rise to a linear trend in ρ_N with time. Extrapolating to t = 0 gives an estimate for the number of PCBM crystals that are nucleated in the first 2 min of annealing when the fully amorphous sample is reverse-quenched from room temperature to above the T_g of PCBM in the blend. The continued nucleation of PCBM crystals with time, combined with the observed polydispersity in crystal sizes after 6 hours of annealing, implies a much faster rate of growth than nucleation for PCBM at 120 °C. Although the kinetics are highly dependent on temperature, the rate of growth also appears to be faster than nucleation for samples annealed at T_{anneal} = 200 °C, based on the polydispersity of crystal sizes in the annealed films.

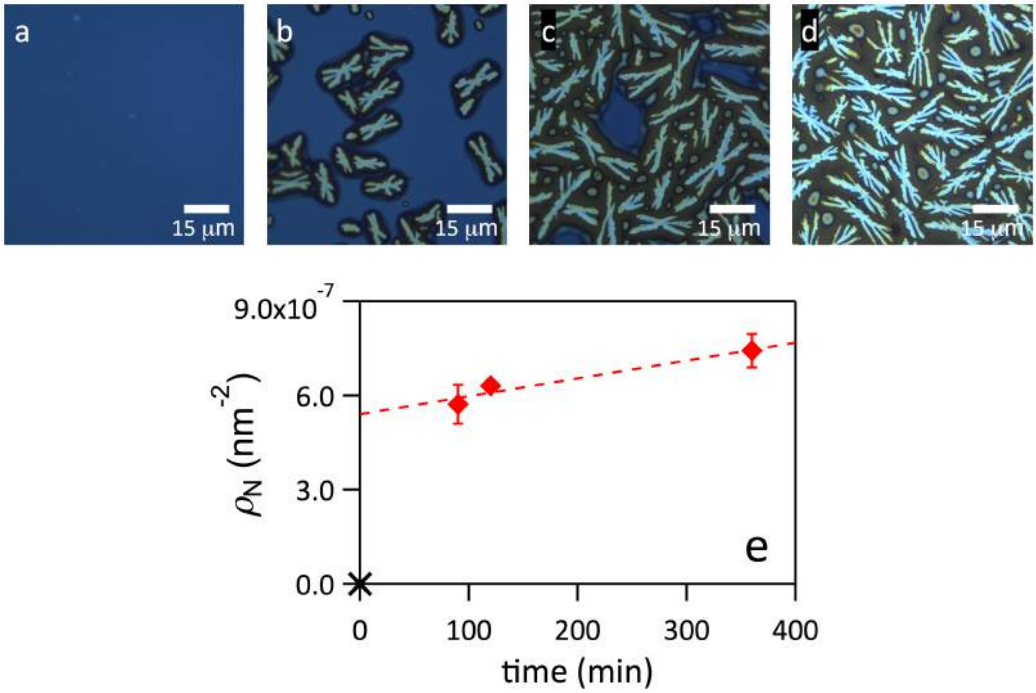

Fig. S12 Time elapsed study of sample B65, a 35:65 blend of P3HT-*b*-P3EHT:PCBM, annealed at 120 °C (under a nitrogen atmosphere). Images show anneal times for: t = 0 (a), t = 90 min (b), t = 2 hours (c), and t = 6 hours (d). The number density of nucleation sites versus time is plotted in (e), the black cross indicates that no crystals were present optically or in GIWAXS at t = 0.

S1.6.2 Microscopic film evolution during thermal anneal.

Time elapsed images for blend B40 show the evolution of surface modulations and PCBM crystals during a standard anneal (200 °C for 6 hours). The film in Figure S13 is initially smooth and changes most dramatically during the first 30 minutes of annealing. Thereafter there is no appreciable change in the number or size of PCBM crystals, however the length scale of the film modulations appears to slowly coarsen during the first 4 hours. The final structure of the film, shown in Figures S13e and f, does not change with further annealing, nor upon cooling.

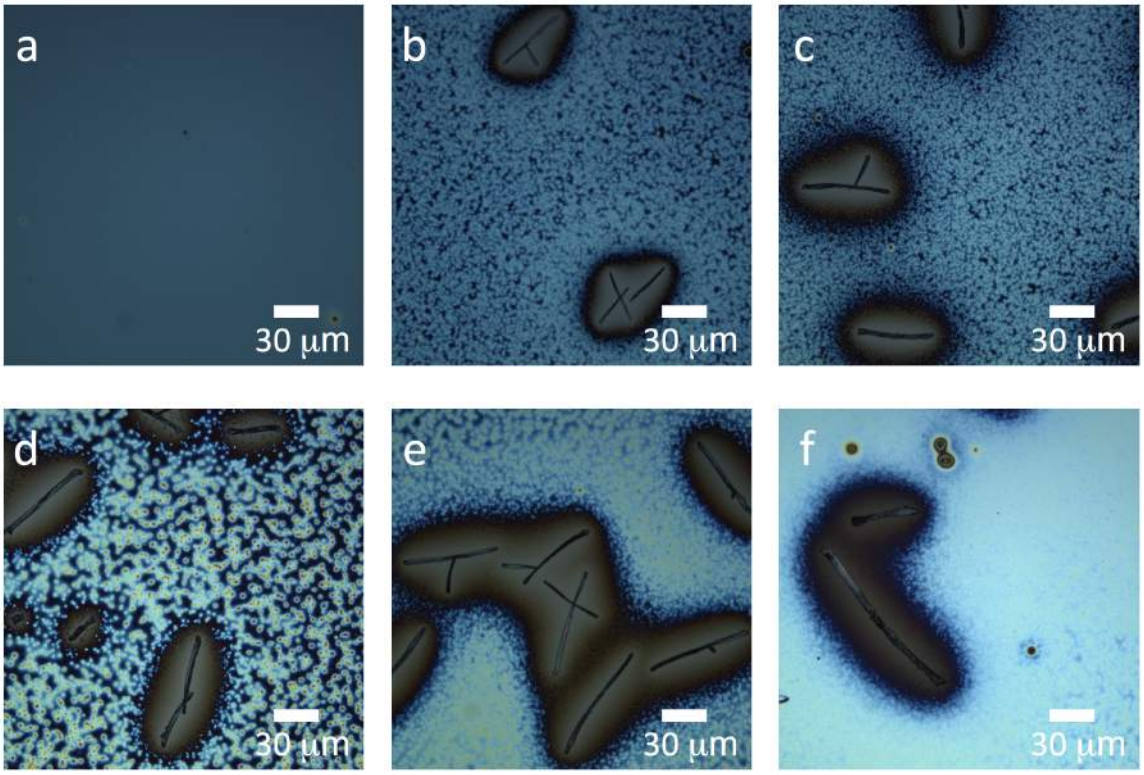

Fig. S13 Time elapsed optical micrographs of B40, a 60:40 blend of P3HT-*b*-P3EHT:PCBM, annealed at 200 °C for: t = 0 (a), t = 30 min (b), t = 2 hours (c), t = 3 hours (d), t = 4 hours (e), t = 6 hours (f).

S1.6.3 Nanostructure evolution during a thermal anneal.

The evolution of nanostructures provides some insight into the mechanism. An intermediate annealing time was examined for blend B40 to elucidate the mechanism of copolymer phase separation. Prior to annealing the film appeared to be a glassy mixture of PCBM and copolymer. The height AFM in Fig. S14 shows a smooth surface, and the phase AFM shows a disordered, very weakly segregated nanophase structure characteristic of a glassy, disordered block copolymer. The sample was annealed under nitrogen for one hour, in a Linkam thermal cell, and rapidly quenched to room temperature to halt annealing. The quench takes two minutes, and is therefore slower than the length scales for nucleation and growth of P3HT crystals. Nanostructures are clearly present in the phase image of the quenched sample. In addition, there are small raised features that are strongly visible in the height image but only weakly visible in the phase, suggesting topographical differences only rather than distinct phases. The final time point is at 6 hours after the film was allowed to cool slowly to room temperature (as for a standard anneal). Not only is the nanostructure highly ordered, small dots are present in both the height and phase images, indicating topographical regions with a higher modulus than the surrounding film. These dots are though to be PCBM nanocrystals that phase separate from the block copolymer during the cooling step because the effective value of x_{misc} is greater at T_{anneal} than at room temperature. They do not appear in the quenched sample, possibly because the kinetics of growth are slower than those of the quench. The images at 1 and 6 hours clearly show the persistence of block copolymer nanostructures on the surface of film undulations.

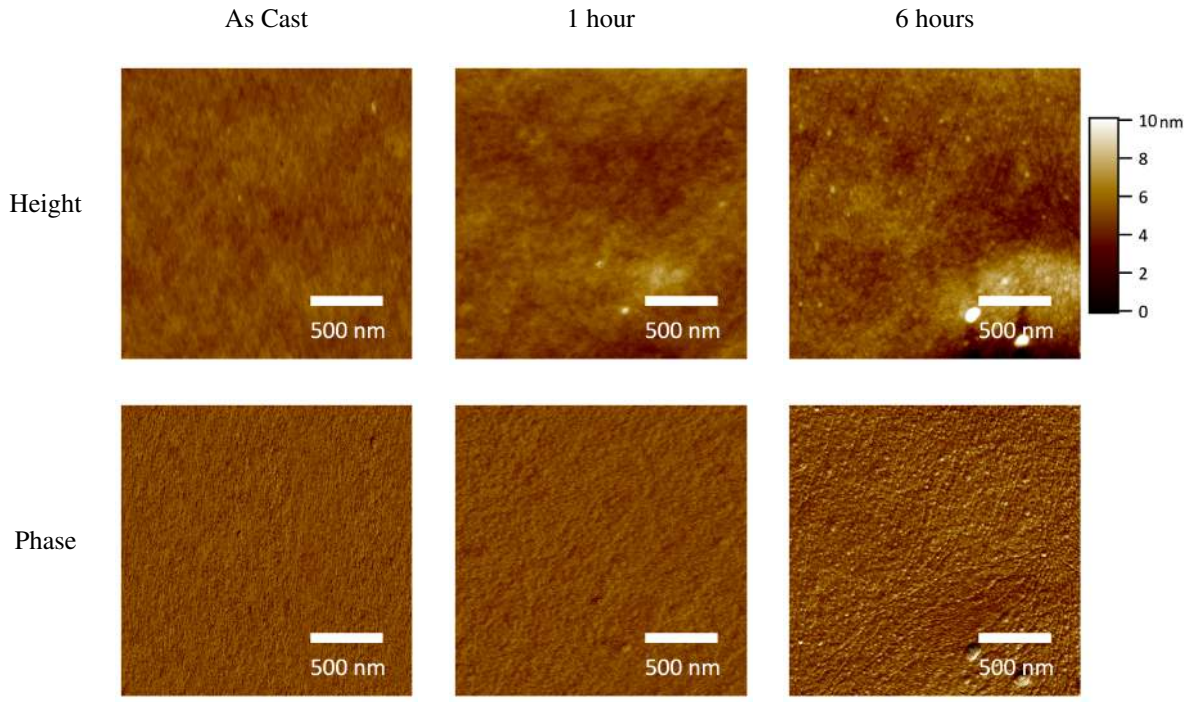

Figure S14. Atomic force micrographs of blend B40, a 60:40 blend of P3HT-*b*-P3EHT:PCBM, after various annealing conditions: The "As Cast" film has not undergone any thermal annealing, the "1 hour" anneal was at 200 °C followed by a rapid quench to room temperature, and the "6 hours" anneal was performed at 200 °C followed by a slow cooling to room temperature. The height scale bar on the right applies to all height images.

S1.6.4 PCBM oxidation in thin films of B65 The fullerene in polymer:fullerene blends is known to oxidise to a species that is far less crystalline than the reduced form of the fullerene[7]. There are multiple locations on the fullerene cage where oxygen can bind, creating a non-uniform population of oxidised PCBM molecules that cannot pack into a regular crystalline lattice [8]. The kinetics of light-induced oxidation are known to be rapid in thin films of polymer:PCBM under the intense light of a microscope objective. Figure S15a shows a photo-oxidised region on a thin film of blend B65, remarkable for the suppression of crystals in the circular light-exposed region. The sample was exposed to a LED microscope light under 50x magnification for 2 minutes, then annealed in the dark for 100 min at 120 °C. The image was acquired using a 5x objective to capture the smooth, circular oxidised region, and the surrounding PCBM crystals in regions not exposed to light. The kinetics of oxidation at ambient conditions are much slower, having no observable effect on crystal structure over the course of two weeks. However, films oxidised over the course of 9 months of storage in a dark, aluminium-foil lined box, packed with sachets of desiccant. Figure S15b shows the complete suppression of PCBM crystals in a film that was oxidised by ageing for 9 months prior to annealing. For comparison, a freshly made and annealed film is shown in Figure S15c, for which the level of oxidation is negligible. Notably, the oxidation only affects the film morphology if the film is not annealed within two weeks of wire bar coating; i.e. films that are annealed shortly after fabrication show no further change in morphology over the 9 months tested.

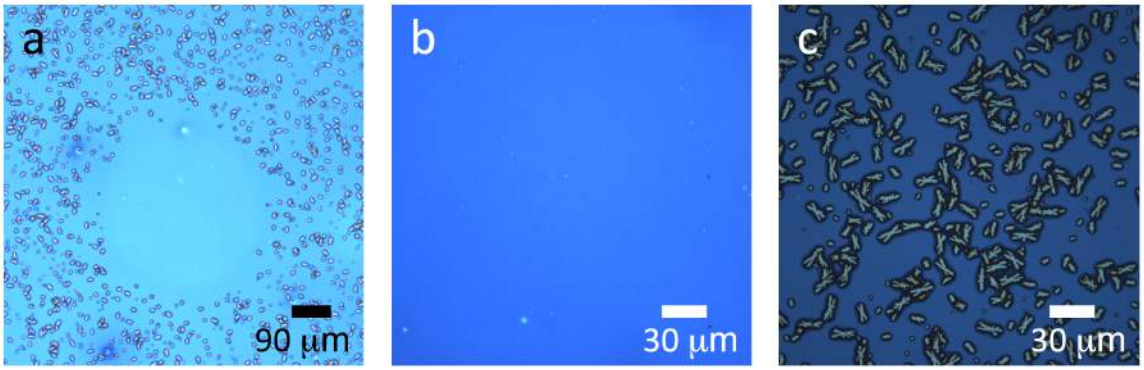

Fig. S15 Optical micrographs of B65, a 35:65 wt % blend of P3HT-*b*-P3EHT:PCBM, subjected to different oxidising conditions: a circular region of the film was exposed to microscope light prior to thermal annealing for 100 min at 120 °C (a), a film was stored in dry, dark conditions for 9 months prior to thermal annealing at 200 °C for 90 min (b), a film was freshly made and annealed on the same day at 120 °C for 90 min (c).

S2 GIWAXS data reduction

S2.1 Q-Calibration

Silver behenate, known to have a crystalline spacing of d_{AgBe} = 5.8380 nm, was used to calibrate the q range of the detector in the transmission configuration, i.e. $\alpha = 0$. The raw spectrum (see Figure S16a) exhibits concentric diffraction rings centred about the incident beam, where $q_{xy} = q_z = 0$. The first five rings in the two-dimension spectrum were fit with five consecutive gaussians in order to extract the coordinates of the beam centre, x_0 and y_0, as well as the distance in pixels, R^*, corresponding to the first order diffraction peak. In q-space, the crystalline spacing of silver behenate is given by $q^* = 2\pi/d_{AgBe} = 1.08nm^{-1}$. Setting $q^* = R^*$ enables a direct calibration of pixels in the q_{xy} direction at all values of grazing incidence, and for pixels in the q_z direction at $\alpha = 0$.

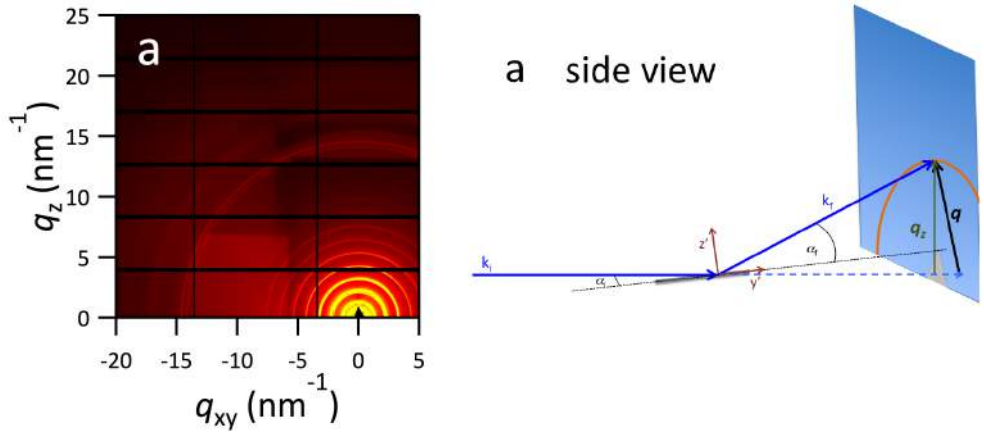

Fig. S16 (a) Raw 2D spectrum for silver behenate measured in transmission geometry ($\alpha = 0$) and (b) schematic of the GIWAXS geometry.

$$I(x,y) = \sum_{i=1}^{5} A_i exp[-\frac{(\sqrt{(x-x_0)^2+(y-y_0)^2} - iR^*)^2}{\sigma^2}] \quad (1)$$

When the grazing incidence angle is nonzero, a correction must be applied to the q_z calibration of the detector. Figure S16b shows the experimental setup in which the incident beam is maintained perpendicular to the detector, and

only the sample is rocked. For simplicity, the schematic depicts a scattering event which takes place entirely in the plane of incidence (i.e. no q_{xy} component). The incident and scattered angles, α_i and α_f, respectively are measured relative to the plane of the substrate, often called the sample frame of reference. It is well known that the component of the momentum transfer vector perpendicular to the sample substrate, q_z is given by Equation 2:

$$q_z = \frac{2\pi}{\lambda}(sin\alpha_i + sin\alpha_f) \tag{2}$$

For an arbitrary vertical displacement on the detector, R_v, the q_z value is known for $\alpha_i = 0$, from which the scattering angle 2θ can be computed. For the case of $\alpha_i = 0$, $\alpha_{f,0} = 2\theta$. Experimentally the sample is tilted by an angle α_i relative to the incident beam, however this is analogous to keeping the sample flat and tilting the incident beam. When α_i is nonzero, the same vertical location on the detector, R_v corresponds to scattering through the angle $\alpha_i + \alpha_{f,0}$, and thus to a slightly larger q-value than for the case when $\alpha_i = 0$. The value of q_z was calculated using equation 2 where α_f was obtained from the measurement of the silver behenate standard and α_i was set by the instrument. Because each sample was aligned with the beam, the error in α_i is negligible.

S2.2 Profile Smoothing

Adjacent detector panels exhibit sharp jumps in the measured intensity of scattered photons, resulting in discontinuities in the radially averaged spectra. Figure S17a highlights this problem, showing the raw two-dimensional spectrum for a silicon wafer in which the colour mapping has been intentionally chosen to emphasise the detector discontinuities. Two white arrows indicate the the most problematic regions on the detector: a nearly-horizontal line mid-panel, where the intensity changes sharply, and above that a semicircular region of higher intensity, probably due to detector damage. These features were apparent in all samples measured. Figure S17b shows the raw silicon meridian in green, clearly exhibiting discontinuities. (Specifically, this is the radially-averaged profile for angles between $\chi = [-\frac{6\pi}{14}, \frac{8\pi}{14}]$.) The standard data reduction procedure is to define a pixel efficiency mask in which each pixel is assigned an efficiency, usually near to unity, to correct for differing detection efficiencies. Lacking a perfectly uniform scattering standard, the silicon spectrum was fit with an empirically chosen log normal decay:

$$I(q_{xy}, q_z) = Aexp\frac{ln(-\sqrt{(\frac{q_z}{q_{z,0}})^2 + (\frac{q_{xy}}{q_{xy,0}})^2})}{\sigma^2} \tag{3}$$

The pixel calibration mask was defined as the ratio of the continuous, log normal model of the silicon data to the actual silicon data, shown in Figure S17c. The image highlights problematic regions that are less evident in the raw spectra. The pixel calibration mask proved unsuitable for quantitative data corrections because the relative intensities of "hot spots" on the detector is not constant between samples, and thus cannot be accounted for by a simple multiplicative factor. Nevertheless, this correction is useful for visually improving the quality of the data.

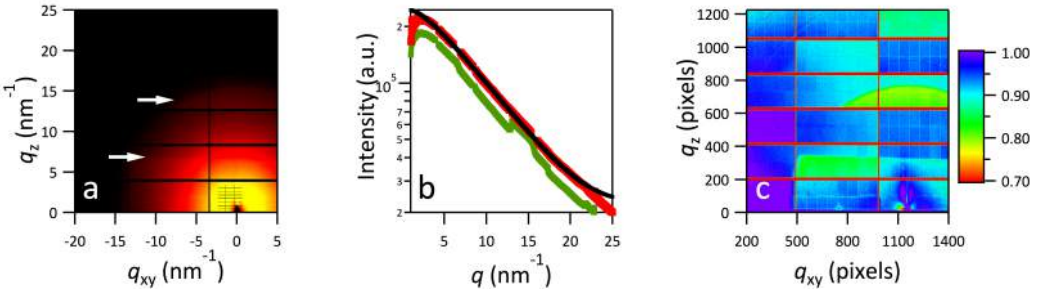

Fig. S17 GIWAXS spectra used for data reduction. (a) Raw spectrum of silicon, arrows indicate problem regions on the detector. (b) Raw silicon meridian (–) showing offsets between detector panels, smoothed profile (–), and log normal fit used to smooth the profile (–). (c) Pixel calibration heat map.

The inability of a single pixel calibration mask to correct samples with scattering invariants moderately different from the silicon wafer implies that the "hot spots" on the detector are a combination of problems: different pixel efficiencies (which can be addressed with a multiplicative pixel calibration), and background scattering due to air and the

slit geometry (generally corrected as an additive empty cell, scaled by the transmission of the sample). To simplify the correction, the raw data were first integrated to produce meridians and equators, and then the one-dimensional profiles were smoothed. Radially integrated spectra for the meridian and equator of each sample were broken into segments corresponding to different panels on the detector. In one case, shown by the arrow in S17a, a sharp discontinuity in the middle of a detector panel was also used as a separation point between segments. An offset value was assigned to each q-segment based on the additive value required to produce a continuous profile for the spectrum of silicon. The red tra shows the smoothed silicon meridian.

The offsets must be scaled for each sample to account for different scattering intensities. The most straightforward scaling factor is the ratio of the sample invariant to the silicon invariant, since the silicon sample was used as the reference for defining the offsets. This strategy was effective for all but the lowest scattering sample, the diblock copolymer, for which the offsets had to be adjusted individually. The smoothed intensity, $I_{smoothed}$ is related to the raw intensity, I_{raw}, by the offset, $\delta(q)$:

$$I_{smoothed}(q) = I_{raw}(q) + \sum_{i=0}^{S} \delta_i(q) \frac{Q_{sample}}{Q_{Si}} \tag{4}$$

The summation is over all S segments, where S = 8 for meridians and S=3 for equators. The q-range for each segment S, along with the base offset applied to that segment, is listed in Table S3 for both meridians and equators.

q-range Å^{-1}	Intensity Offset (a.u.)
0.1 - 0.386	-5988
0.431 - 0.608	-3003
0.690 - 0.843	3932
0.869 - 1.287	3006
1.303 - 1.532	-6006
1.599 - 1.737	-542
1.738 - 2.172	1200
2.181 - 2.500	0

Table S3 Intensity offsets for q-ranges

S2.3 Silicon background subtraction

The large power-law slope of the samples is clearly an artefact of the scattering due to the silicon substrate, specifically the rough silicon oxide layer on the substrate (as a perfectly smooth sample would exhibit only a specular reflection). A log normal fit to the silicon was chosen based on goodness-of-fit rather than for any fundamental reason. As with transmission mode scattering, e.g. SAXS, the silicon substrate was treated as the "empty cell" and subtracted from the smoothed sample intensity. The transmission coefficient, T, accounts for light that is refracted into the thin film and dissipated as heat or scattered into a q-range outside the one of interest. We were unable to directly measure the transmission coefficients, so transmissions were chosen based on the requirement that the ratio of the invariants of the sample to an arbitrary reference must be constant before and after the transmission correction. The scattering invariant is different for each sample because it depends on the scattering volume and the scattering power, both of which change as different amounts of PCBM are added to the samples. However the ratio of the invariant of each sample to to the arbitrary reference remains constant when data reductions are correctly applied. This requirement ensures consistency between different samples measured at the same integration angle.

$$I_{corr} = I_{smoothed} - T I_{Si} \tag{5}$$

PCBM was chosen as the reference sample because it scattered most strongly. The transmission coefficient for PCBM was chosen by selecting the value for which the meridian profile exhibited a constant baseline for the amorphous scattering peak around q = 14 nm^{-1}, consistent with previously reported data[9]. Although this choice is some-

what arbitrary, the requirement for self-consistency between samples enables rigorous comparison. The transmission coefficient for each sample was calculated by trial and error subject to the constraint:

$$\frac{Q_{sample,smoothed}}{Q_{PCBM,smoothed}} = \frac{Q_{sample,corrected}}{Q_{PCBM,corrected}} \tag{6}$$

The transmissions calculated for the meridians were then applied to the equators by making the assumption that transmission is isotropic for the samples studied. To test the self-consistency of this approach, the invariant for the equator of each sample (corrected by using the transmission calculated for the corresponding meridian) was plotted against the raw invariant for the same sample. The eight points shown in Figure S18correspond to the four diblock:PCBM blends and to the four neat components: PCBM, diblock, P3HT, and P3EHT. Clearly a linear trend emerges, indicating that the correction applied has systematically addressed all the samples.

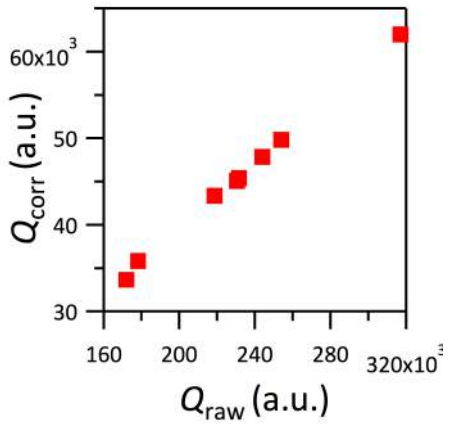

Fig. S18 Self-consistency check comparing the scattering invariant of the systematically corrected data, Q_{corr} with the raw invariant, Q_{raw}.

References

1 R. S. Loewe, P. C. Ewbank, J. Liu, L. Zhai and R. D. McCullough, *Macromolecules*, 2001, **34**, 4324–4333.

2 V. Ho, B. W. Boudouris and R. A. Segalman, *Macromolecules*, 2010, **43**, 7895–7899.

3 Y. Zhang, K. Tajima and K. Hashimoto, *Macromolecules*, 2009, **42**, 7008–7015.

4 J. Zhao, A. Swinnen, G. Van Assche, J. Manca, D. Vanderzande and B. Van Mele, *The Journal of Physical Chemistry B*, 2009, **113**, 1587–1591.

5 S. Malik and A. K. Nandi, *Journal of Polymer Science Part B: Polymer Physics*, 2002, **40**, 2073–2085.

6 M. T. Rispens, A. Meetsma, R. Rittberger, C. J. Brabec, N. S. Sariciftci and J. C. Hummelen, *Chemical Communications*, 2003, 2116–2118.

7 H. C. Wong, A. M. Higgins, A. R. Wildes, J. F. Douglas and J. a. T. Cabral, *Advanced materials*, 2013, **25**, 985–991.

8 P. C. Eklund, A. M. Rao, P. Zhou, Y. Wang and J. M. Holden, *Thin Solid Films*, 1995, **257**, 185–203.

9 N. Kayunkid, S. Uttiya and M. Brinkmann, *Macromolecules*, 2010, **43**, 4961–4967.